EDGE ARTICLE

Check for updates

Atomic-level engineering of single Ag^{1+} site distribution on titanium–oxo cluster surfaces to boost CO_2 electroreduction†

Ru-Xin Meng,‡[a] Lan-Cheng Zhao,‡[b] Li-Pan Luo,[c] Yi-Qi Tian,[a] Yong-Liang Shao,[d] Qing Tang, [iD] *[c] Likai Wang, [iD] *[b] Jun Yan [iD] [a] and Chao Liu [iD] *[a]

Precise control over the distribution of active metal sites on catalyst surfaces is essential for maximizing catalytic efficiency. Addressing the limitations of traditional cluster catalysts with core-embedded catalytic sites, this work presents a strategy to position catalytic sites on the surfaces of oxide clusters. We utilize a calixarene-stabilized titanium–oxo cluster ($Ti_{12}L_6$) as a scaffold to anchor Ag^{1+} *in situ*, forming the unique nanocluster $Ti_{12}Ag_{4.5}$ with six surface-exposed Ag^{1+} sites. The *in situ* transformation from $Ti_{12}L_6$ into $Ti_{12}Ag_{4.5}$ clusters was traced through mass spectrometry, revealing a solvent-mediated dynamic process of disintegration and reassembly of the $Ti_{12}L_6$ macrocycle. The unique $Ti_{12}Ag_{4.5}$ cluster, featuring a surface-exposed catalytic site configuration, efficiently catalyzes the electroreduction of CO_2 to CO over a broad potential window, achieving CO faradaic efficiencies exceeding 82.0% between −0.4 V and −1.8 V. Its catalytic performance surpasses that of bimetallic Ti_2Ag_2, which features a more conventional design with Ag^{1+} sites embedded within the cluster. Theoretical calculations indicate that the synergy between the titanium–oxo support and the single Ag^{1+} sites lowers the activation energy, facilitating the formation of the *COOH intermediate. This work reveals that engineered interactions between active surface metal and the oxide support could amplify catalytic activity, potentially defining a new paradigm in catalyst design.

Introduction

Within the intricate sphere of catalysis, the sophisticated interplay of size, morphology, and structural attributes of materials is recognized for its profound influence on catalytic efficacy.[1–4] Recently developed single-atom catalysts (SACs), with isolated metal atoms dispersed on solid supports, are garnering significant attention due to their exceptional catalytic efficiency and ability to maximize the utilization of metal atoms.[5–9] Oxide-supported SACs, in particular, are among the most thoroughly investigated systems.[10] Advances in the fabrication of these materials are noteworthy, but achieving uniform dispersion of

catalytic sites on oxide substrates remains a significant challenge.[11] This requires not only advanced synthesis techniques but also sophisticated characterization methods.[12] The complexity is further exacerbated by the absence of detailed atomic structures, which obscures the analysis of the metal coordination environment—a pivotal factor in determining the performance of these catalyst systems.[13–15]

To effectively tackle these challenges, it is crucial to develop molecular analogues for oxide-supported single-atom materials. Recent advances in TiO_2 analogues,[16–19] particularly through the development of crystalline titanium oxide clusters (TOCs), have facilitated comprehensive investigations of TiO_2 structures and reactivities at the molecular level.[20–24] These TOCs, when modified with catalytically active single metals, hold promise as effective molecular mimics for oxide-supported SACs. However, heterometal-doped TOCs are typically created *via* a one-pot solvothermal method, with heterometal sites embedded deep within the cluster core, often in fully coordinated states.[25–29] Such configurations limit the interactions with reactants, exposing a significant shortfall in their capacity to act as true molecular proxies. This insight highlights the urgent need for a new class of crystalline, cluster-stabilized single-atom materials, designed to more precisely emulate the structural and reactive properties of oxide-supported SACs at a molecular level.[30,31]

[a] *College of Chemistry and Chemical Engineering, Central South University, Changsha 410083, Hunan, P. R. China. E-mail: chaoliu@csu.edu.cn*

[b] *School of Chemistry and Chemical Engineering, Shandong University of Technology, Zibo 255049, Shandong, P. R. China. E-mail: lkwangchem@sdut.edu.cn*

[c] *College of Chemistry and Chemical Engineering, Chongqing University, Chongqing, 400044, P. R. China. E-mail: qingtang@cqu.edu.cn*

[d] *School of Chemistry and Chemical Engineering, Lanzhou University, Lanzhou, 730000, P. R. China*

Here, we present an approach designed to strategically place catalytic Ag^{1+} sites on the surfaces of oxide clusters (Scheme 1). Employing thiacalix[4]arene (TC4A) as a protective ligand,[32–38] we meticulously engineered a titanium–oxo macrocycle, $Ti_{12}L_6$, through a one-step solvothermal method, which is enriched with surface O and S sites. We utilized $Ti_{12}L_6$ as a scaffold for the *in situ* loading of Ag^{1+} ions, revealing a solvent-mediated assembly process through mass spectrometry. In *N,N*-dimethylformamide (DMF) solution, the scaffold undergoes decomposition under the cleavage of Ag^{1+} ions; however, in acetonitrile, the scaffold remains stable and coordinates six accessible single Ag^{1+} sites on the cluster surface, ultimately transforming into a $Ti_{12}Ag_{4.5}$ cluster. $Ti_{12}Ag_{4.5}$ has proven to be an exceptional catalyst for the electrochemical reduction of CO_2, exhibiting superior reactivity and CO selectivity compared to its bimetallic counterpart, Ti_2Ag_2, which possesses a more conventional structure with Ag^{1+} sites embedded within the cluster matrix. Notably, $Ti_{12}Ag_{4.5}$ exhibits high selectivity for CO across a wide voltage range, with CO faradaic efficiency (FE_{CO}) consistently exceeding 82.0% from -0.4 V to -1.8 V *vs.* RHE, reaching a peak FE_{CO} of 92.7%. At an overpotential of ~-1.4 V, the system remained stable for continuous electrolysis over 11 h with a CO partial current density exceeding 100.0 mA cm^{-2}, while the FE_{CO} consistently remains above 85.0%. We elucidated the reaction path using *in situ* ATR-SEIRAS technology and comprehensively calculated the Gibbs free energy changes for each elementary step of CO_2 conversion to CO, highlighting the critical contribution of exposed Ag centers to the observed catalytic prowess.

Results and discussion
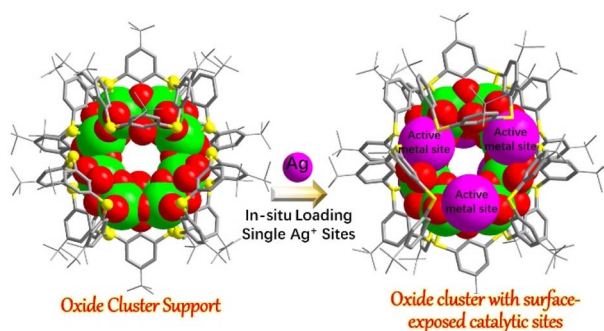
One-step synthesis of titanium–oxo macrocyclic carriers

The synthetic route commenced with the reaction of $Ti(O^iPr)_4$ with TC4A in a solvent blend of $CH_3CN/CHCl_3$, maintained at 80 °C for three days. This process yielded a turbid yellow liquid. Extending the reaction duration by introducing acetone and continuing incubation at 80 °C for an additional three days led to the crystallization of yellow rhomboid crystals of $Ti_{12}L_6$. Interestingly, this reaction exhibits a high sensitivity to temperature changes. Upon heating to 130 °C, certain sulfur sites in TC4A oxidize, leading to the emergence of two distinct

Scheme 1 Schematic representation of the cluster assembly featuring a Ti–oxo core with surface-exposed Ag^{1+} catalytic sites.

TOCs, Ti_8L_6 and Ti_8L_5. SCXRD analysis revealed that the $Ti_{12}L_6$ cluster has the composition of $\{H_6Ti_{12}O_{18}(HTC4A)_6\}$, featuring a core–shell architecture where a central Ti–oxo macrocycle is encapsulated by six TC4A molecules. $Ti_{12}L_6$ consists of six $\{Ti_2O(TC4A)\}$ units interconnected by twelve μ_2-O^{2-} (Fig. 1A). TC4A adopts a mono-cone configuration, coordinating with two Ti^{4+} through three phenoxide groups and two S atoms, thereby forming the $\{Ti_2O(TC4A)\}$ units. These units are geometrically arranged in a triangular pattern, bridged by five μ_2-O linkages to form a trimeric $\{Ti_6(TC4A)_3\}$. This trimer further aggregates into the hexameric $\{Ti_{12}(TC4A)_6\}$ structure *via* the integration of two additional μ_2-O^{2-} ions (Fig. 1B). This configuration yields a "donut" shape with an outer diameter of 3 nm, representing the largest TC4A-stabilized TOC reported to date (Fig. 1C). The structure of Ti_8L_6 closely resembles that of $Ti_{12}L_6$, with a central Ti_8O_8 ring encircled by six TC4A molecules (Fig. 1D). In contrast, the core of Ti_8L_5 consists of a Ti_8O_{10} cluster, surrounded by five TC4A molecules arranged in a pentagonal bipyramidal configuration. In both structures, some of the TC4A molecules undergo oxidation, with one or two sulfur sites being converted to S=O groups. Additionally, each structure has two Na^+ ions adsorbed on its surface.

Solvent-mediated assembly of $Ti_{12}Ag_{4.5}$ clusters

The surfaces of this series of calixarene-stabilized TOCs are endowed with abundant O/S sites. Specifically, in Ti_8L_6 and Ti_8L_5, these sites facilitate the adsorption of Na^+ onto the cluster surfaces. This characteristic has inspired us to utilize these clusters as carriers for positioning Ag^{1+} ions. In our preliminary studies, we attempted to directly introduce Ag(I) salt into the reaction mixture for these clusters, but this approach resulted in the formation of crystals of Ti_2Ag_2 (Fig. 2A). Ti_2Ag_2 is a typical bimetallic cluster, with two Ag^{1+} and two Ti^{4+} ions arranged in a quadrilateral configuration, sandwiched between two oxidized-TC4A ligands (Fig. 2B). Each Ag^{1+} site maintains a coordination number of six, with the Ag^{1+} seamlessly integrated into the cluster core, effectively shielded from external exposure (Fig. 2C). The composition of Ti_2Ag_2 was determined using electrospray ionization mass spectrometry (ESI-MS) (Fig. S28†), which revealed a +1 signal at $m/z = 1794.18$, corresponding to the species $[HTi_2Ag_2O(O-TC4A)_2]^+$.

Interestingly, using $Ti_{12}L_6$ crystals in reactions with Ag(I) salts yielded distinctly different outcomes. Introducing Ag_2SO_4 into DMF solution along with $Ti_{12}L_6$ crystals and allowing the mixture to react at 80 °C for three days resulted in the formation of the known clusters Ti_2Ag_2-DMF and Ti_2Ag_4.[34] Subsequently, by switching the solvent to CH_3CN, rhombic $Ti_{12}Ag_{4.5}$ crystals were obtained, emphasizing the critical role of solvent selection in steering the chemical pathway. Ti_2Ag_2-DMF and Ti_2Ag_4 have typical bimetallic configurations, with two or four Ag^{1+} ions embedded between two $\{Ti(TC4A)\}$ units. In contrast, in $Ti_{12}Ag_{4.5}$, multiple Ag^{1+} ions are effectively anchored onto the surface of the Ti_{12} core without altering its intrinsic structure. SCXRD analysis revealed the structure of $Ti_{12}Ag_{4.5}$ to be $[H_{1.5}$-$Ti_{12}Ag_{4.5}O_{18}(HTC4A)_6(CH_3CN)_4]$, with the cluster containing three crystallographically distinct sites for Ag. Structural
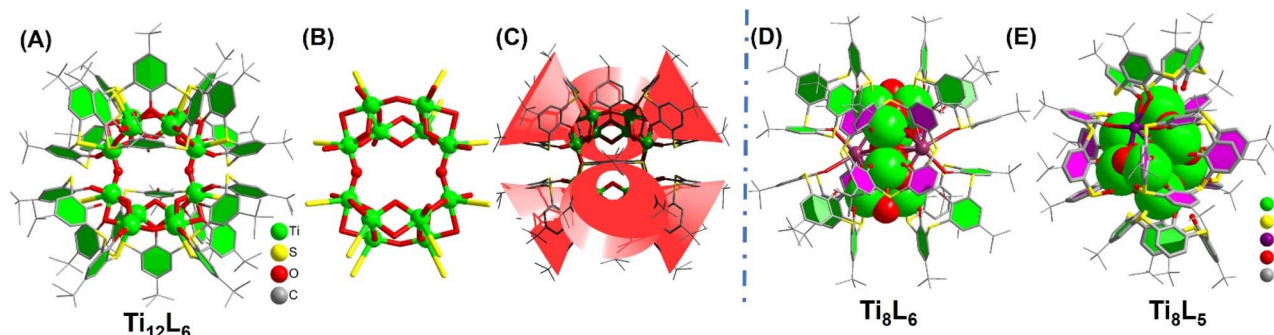
Fig. 1 (A) The overall structure of $Ti_{12}L_6$; (B) the $Ti_{12}O_{18}$ core in $Ti_{12}L_6$; (C) the polyhedral arrangement of six calix moieties in $Ti_{12}L_6$; (D) the overall structure of Ti_8L_6; (E) the overall structure of Ti_8L_5.
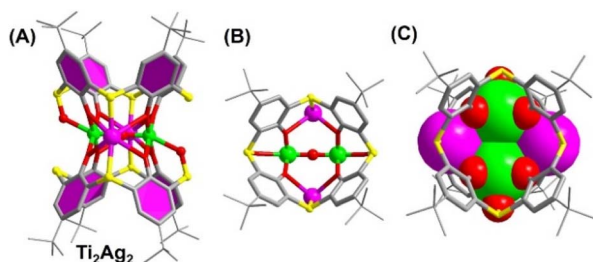

Fig. 2 (A) The overall structure of Ti_2Ag_2; (B) coordination mode of oxidized TC4A in Ti_2Ag_2. (C) Comparison of the positions of the Ag and Ti sites in Ti_2Ag_2.

analysis demonstrated that the Ti–oxo core of $Ti_{12}Ag_{4.5}$ closely mirrors the macrocyclic structure of $Ti_{12}L_6$, albeit with minor deviations (Fig. 3A). The Ag^{1+} sites are symmetrically divided and positioned on both the upper and lower facets of the Ti–oxo macrocycle (Fig. 4B). Ag1 and Ag2, coordinated through phenoxide, sulfur, and $\mu-O_2^{2-}$, are placed between two TC4A ligands, exhibiting coordination numbers of 3 and 4, respectively. The distances between Ag1/Ag2 and the Ti–oxo core range from 2.392 to 2.607 Å. Notably, the Ag3 site, with an O_3N_2 coordination environment, is defined by two phenoxide groups, one $\mu-O_2^-$, and two CH_3CN, with Ag–O bond lengths ranging from 2.649 to 2.774 Å and Ag–N distances of 2.056 and 2.215 Å. The

spatial arrangement of the Ag sites, especially the Ag3 sites proximal to the cluster surface as depicted in Fig. 3C, highlights their potential as catalytically active sites. This is particularly significant given the labile nature of the CH_3CN ligand, which may facilitate dynamic catalytic processes. Sites Ag1 and Ag2 exhibit full occupancy, while Ag3 displays a partial occupancy of 0.25. As a result, the average number of Ag sites in the cluster is 4.5, which is confirmed by the mass spectrometry analysis of $Ti_{12}Ag_{4.5}$. Matrix-assisted laser desorption/ionization time-of-flight mass spectrometry (MALDI-TOF-MS) analysis reveals six distinct peaks with a mass difference of 107.86, corresponding to the ion $\{H_4Ti_{12}Ag_6O_{16}(TC4A)_6(CH_2Cl_2)\}^+$ (Fig. 3D) ($x = 1$–6). This pattern suggests that the cluster contains six Ag sites, which can sequentially detach under ionization conditions. Additionally, the atomic ratio of Ag to Ti in the cluster, as determined by ICP analysis, is 2.63, which is in excellent agreement with the theoretical value of 2.66 (Table S2†).

From the above results, it is evident that the solvent choice significantly influences the reaction pathway of $Ti_{12}L_6$ with Ag(I) salts; CH_3CN primarily leads to $Ti_{12}Ag_{4.5}$, whereas solvents like DMF result in different structures of Ti_2Ag_2-DMF and Ti_2Ag_4. The significant impact of seemingly minor variations in solvent choice on the synthesis outcomes is fascinating. To elucidate the formation mechanism of $Ti_{12}Ag_{4.5}$, its evolutionary process was monitored using ESI-MS.[39] Time-resolved ESI-MS analysis of the reaction mixture, containing $Ti_{12}L_6$ crystals and Ag_2SO_4 in
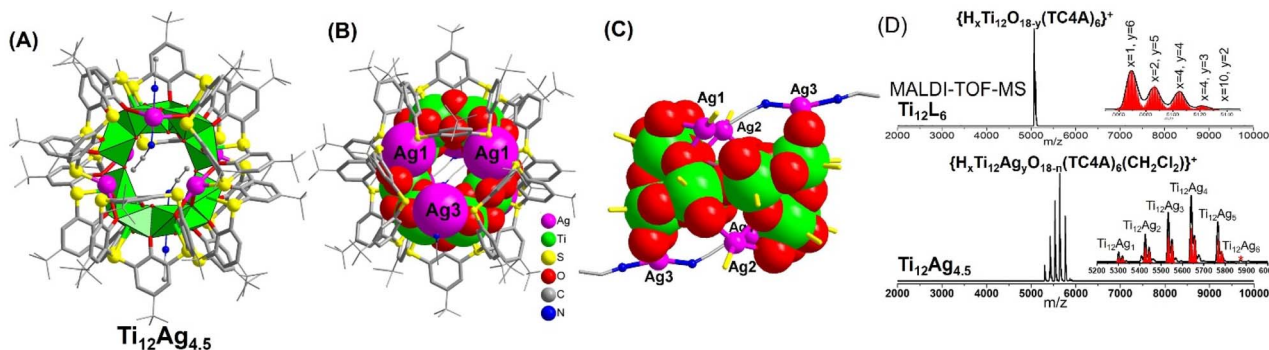

Fig. 3 (A) The overall structure of $Ti_{12}Ag_{4.5}$; (B) space-filling model of the structure of $Ti_{12}Ag_{4.5}$, highlighting the exposed Ag atoms on the surface; (C) bonding mode of six Ag^{1+} sites to the titanium oxide core; (D) positive-mode MALDI-TOF-MS of $Ti_{12}L_6$ and $Ti_{12}Ag_{4.5}$ in CH_2Cl_2 solution.
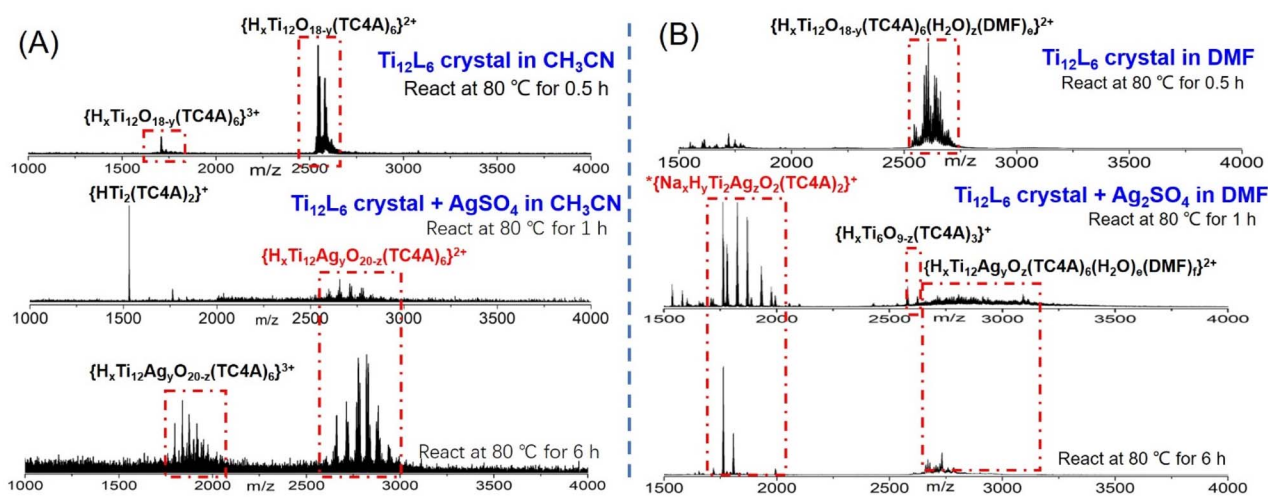
Fig. 4 Time-dependent ESI-MS for the reaction of the $Ti_{12}L_6$ crystals and Ag_2SO_4 in CH_3CN (A) or DMF (B) solution at 80 °C at 0 h, 1 h and 6 h.

CH$_3$CN, captured data at various intervals (Fig. 4A). Initially, ESI-MS detected two principal signal sets corresponding to the +2 and +3 charge states of $\{H_xTi_{12}O_{18-y}(TC4A)_6\}$, indicating that $Ti_{12}L_6$ maintained its integrity in the early stages of the reaction. After heating at 80 °C for one hour, new signals emerged, with a strong peak corresponding to $\{HTi_2(TC4A)_2\}^+$, resulting from the fragmentation of $Ti_{12}L_6$. Additionally, subtle signals in the m/z range of 2000–2500, likely representing $\{Ti_{12}Ag_xO_{20-z}(TC4A)_6\}^{2+}$, were observed. By the six-hour mark, the spectrum displayed distinct signal sets aligned with the +2 and +3 charge states of the $\{H_xTi_{12}Ag_yO_{20-z}(TC4A)_6\}$ species, indicating a complete transformation of $Ti_{12}L_6$ into $Ti_{12}Ag_{4.5}$.

Conversely, in a DMF environment, ESI-MS revealed a completely different reaction scenario (Fig. 4B). Initially, $Ti_{12}L_6$ also maintained its structure in DMF (Fig. S34†). One hour post Ag(I) salt introduction, ESI-MS revealed the breakdown of the macrocycle, detecting $\{H_xTi_6O_z(TC4A)_3\}^+$ and $\{H_xTi_2O_z(TC4A)_2\}^+$ species. Notably, the emergence of $\{H_xTi_2Ag_yO_z(TC4A)_2\}^+$ ($x = 2$–4) clarified the formation of Ti_2Ag_4 and Ti_2Ag_2-DMF clusters. By the six-hour mark, these signals intensified significantly, highlighting the progressive formation of these clusters in the DMF solution.

These findings indicate that the synthesis of $Ti_{12}Ag_{4.5}$ is not merely a simple process of Ag^{1+} adsorption onto the $Ti_{12}L_6$ carrier. Instead, it involves a complex sequence of fragmentation and subsequent reassembly (Fig. 5). Under solvothermal conditions, the $Ti_{12}L_6$ framework undergoes a fragmentation process, resulting in the formation of $\{Ti_2O(TC4A)\}$ units. A dynamic equilibrium forms between the larger $\{Ti_{12}O_{12}(TC4A)_6\}$ structure and these smaller $\{Ti_2O(TC4A)\}$ units. In the presence of CH$_3$CN solvent, during the reassembly phase, these $\{Ti_2O(TC4A)\}$ fragments coordinate with Ag^{1+} ions, facilitating the formation of $Ti_{12}Ag_{4.5}$. Conversely, using DMF as the solvent leads to a transformation of the $\{Ti_2O(TC4A)\}$ units into more complex $\{Ti_2O(TC4A)_2\}$ structures. These structures then complex with Ag^{1+} ions to form Ti_2Ag_2-DMF and Ti_2Ag_4, highlighting a distinct synthetic pathway that is significantly influenced by the choice of solvent.

Electrochemical CO$_2$ reduction

Ag-based nanoclusters are optimal catalysts for electrocatalytic CO$_2$ reduction reactions.[40–42] Tuning the coordination environment of Ag sites within the clusters is a key strategy to boost their catalytic activity and tune the selectivity for CO production.[43–51] From the structural comparison provided, it is clear that the distribution of Ag sites in the two Ti–Ag clusters, $Ti_{12}Ag_{4.5}$ and Ti_2Ag_2, is significantly different. For bimetallic Ti_2Ag_2, Ag^{1+} and Ti^{4+} sites are indistinguishably mixed within the core of the cluster. In contrast, Ti^{4+} sites of $Ti_{12}Ag_{4.5}$ are embedded in the Ti–oxo core, while Ag^{1+} sites are strategically distributed across the cluster surface. These structural differences between $Ti_{12}Ag_{4.5}$ and Ti_2Ag_2 provide a unique platform for investigating how variations in the Ag environments affect their catalytic activity.[52,53]

Powder X-ray diffraction (PXRD) analysis shows that the $Ti_{12}Ag_{4.5}$ crystal maintains its crystalline structure even after exposure to a highly alkaline 1 M KOH solution for 24 hours (Fig. S35†). Given the resilience of $Ti_{12}Ag_{4.5}$, its eCO$_2$RR activity was assessed in a three-compartment flow cell with 1 M KOH as the electrolyte. Linear sweep voltammetry (LSV) results
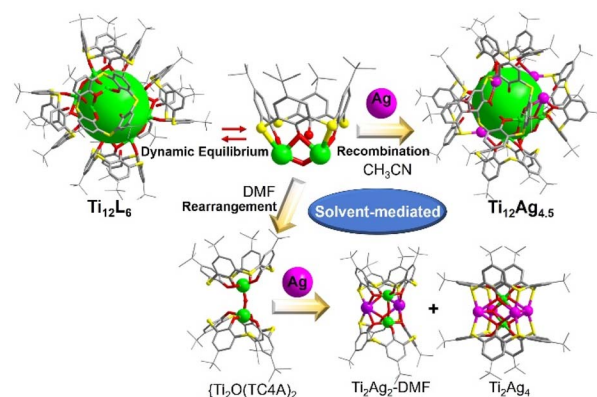

Fig. 5 Schematic diagram illustrating the solvent-mediated self-assembly process transitioning from $Ti_{12}L_6$ to $Ti_{12}Ag_{4.5}$.

indicated a significantly higher current density and more positive onset potential for both the **Ti$_{12}$Ag$_{4.5}$** and **Ti$_2$Ag$_2$** clusters in the CO$_2$ flow electrolyzer compared to the N$_2$-purged system, confirming their CO$_2$ reduction capability, as illustrated in Fig. 6A. Gas chromatography detected only CO and H$_2$ as products, with no other liquid products identified by ^{1}H NMR spectroscopy (Fig. S39†). Control experiments under N$_2$-saturated conditions yielded no carbon-reduction products. Isotopic tracing experiments with ^{13}CO$_2$ through GC-MS confirmed the production of ^{13}CO ($m/z = 29$) (Fig. S40†). Additionally, the primary electrocatalytic product of the **Ti$_{12}$L$_6$** catalyst was identified as H$_2$, indicating that the Ag^{1+} components of these clusters predominantly drive the catalytic activity (Fig. S37†).

Fig. 6B and C illustrate the trends in product distribution across varying potentials for two distinct clusters. In a CO$_2$-saturated environment, **Ti$_{12}$Ag$_{4.5}$** consistently exhibits a high FE$_{CO}$ production, maintaining over 82.0% across an extensive potential range from −0.4 V to −1.8 V vs. RHE, peaking at 92.7% at a higher potential of −1.4 V (Table S3†). However, for **Ti$_2$Ag$_2$**, the predominant reaction between −0.6 V and −1.0 V is CO$_2$ reduction, reaching its highest FE$_{CO}$ of 85.1% at −0.8 V. Beyond this, the reaction is largely overtaken by H$_2$ evolution in the potential range from −1.2 to −1.8 V, leading to a progressive decline in FE$_{CO}$ as potential increases. At −1.8 V, the FE$_{CO}$ of **Ti$_2$Ag$_2$** plummets to merely 21.2%, whereas **Ti$_{12}$Ag$_{4.5}$** still manages to maintain an FE$_{CO}$ of 83.25%. Additionally, the CO partial current density (J_{CO}) for both clusters was also analyzed (Fig. 6D). The J_{CO} for **Ti$_{12}$Ag$_{4.5}$** reached an impressive 130.1 mA cm^{-2} at −1.8 V, which is above 2.4 times greater than that of **Ti$_2$Ag$_2$**. This comparative analysis emphasizes the pronounced differences in catalytic efficiencies between two clusters, attributing **Ti$_{12}$Ag$_{4.5}$**'s superior performance to its unique structural configuration and effective Ag^{1+} site utilization.

Electrocatalytic stability is a key indicator for evaluating the performance of electrocatalysts in the eCO$_2$RR. We employed PXRD to analyze the reduction of Ag$^+$ in **Ti$_{12}$Ag$_{4.5}$** after reaction at different applied voltages (Fig. S44†). PXRD analysis reveals that the catalyst remains stable when the applied voltage is below −1.8 V. However, when the voltage exceeds −1.8 V, signals corresponding to Ag nanoparticles appear, indicating the reduction of Ag$^+$ to metallic Ag. To further evaluate the durability of the catalyst, we conducted a rigorous 11-hour chronoamperometric test at −1.4 V. During this process, the current density remained above 100 mA cm^{-2}, and the FE for CO remained stable above 85.0% (Fig. 6E). Additionally, ESI-MS analysis of the catalysts after electrolysis showed a signal for the $\{H_x Ti_{12}Ag_6 O_{18-z}(TC4A)_6\}^{2+}$ species, confirming that the structural integrity of the **Ti$_{12}$Ag$_{4.5}$** catalyst was maintained (Fig. S45†). Further characterization by transmission electron microscopy, X-ray photoelectron spectroscopy, and infrared spectroscopy showed that the catalyst maintained its chemical composition and structural stability during the electrolysis process (Fig. S47–S49†). Differential pulse voltammetry (DPV) measurements reveal that the electrochemical gap of **Ti$_{12}$Ag$_{4.5}$** is 1.91 V (Fig. S50†), which is greater than the 1.32 V observed for **Ti$_2$Ag$_2$**. This larger electrochemical gap further suggests enhanced stability of **Ti$_{12}$Ag$_{4.5}$** during the electrocatalytic process. The stability of Ag$^+$ in the **Ti$_{12}$Ag$_{4.5}$** clusters can be attributed to the strong electronic and structural stabilization provided by the Ti–oxo support. This unique characteristic not only preserves the active sites but also prevents the competitive reduction of Ag$^+$, thereby enhancing the suitability of these clusters for CO$_2$ reduction.

The hypothesized mechanism for CO$_2$ reduction to CO using Ag-based catalysts follows the pathway: CO$_2$(g) → *COOH → *CO → CO(g).[54–57] To validate this mechanism, we utilized in situ electrochemical attenuated total reflection surface-enhanced infrared absorption spectroscopy (ATR-SEIRAS). This technique allows for real-time monitoring of the absorption of evanescent waves by substances on the catalyst surface, providing direct insight into the reaction dynamics. We set the potential range from −0.5 V to −1.3 V and monitored changes in absorption peaks with **Ti$_{12}$Ag$_{4.5}$** and **Ti$_2$Ag$_2$** as the electrocatalysts (Fig. 6F). The spectra display similarities, including
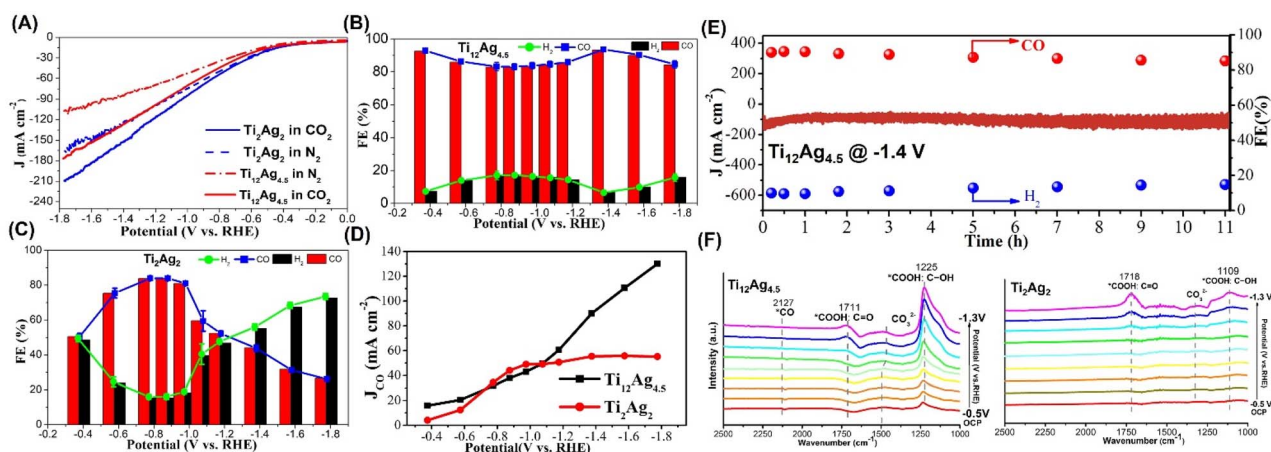

Fig. 6 (A) LSV of samples in N$_2$ or CO$_2$ saturated 1 M KOH solution; (B) FE values of **Ti$_{12}$Ag$_{4.5}$** at different voltages; (C) FE values of **Ti$_2$Ag$_2$** at different voltages; (D) CO partial current density (j_{CO}); (E) I−t test and FE$_{CO}$ values of **Ti$_{12}$Ag$_{4.5}$** at −1.4 V vs. RHE in different time periods; (F) the ATR-SEIRAS results from 2500 to 1000 cm^{-1} of **Ti$_2$Ag$_2$** and **Ti$_{12}$Ag$_{4.5}$**.

a pronounced peak at 1225 cm^{-1}, attributed to C–OH stretching in *COOH, which intensifies with increasing voltage. Another peak at 1711 cm^{-1}, corresponding to C=O stretching in *COOH, also increases in intensity from −0.5 V to −1.3 V, suggesting a rise in the surface coverage of *COOH species with increasing voltage.[58,59] Additionally, a weak signal at 2127 cm^{-1}, attributed to the Ag–*CO vibration mode, indicates the presence of *CO adsorbed on the catalyst surface, especially at lower potentials where the *CO band intensity shows a slight increase. Notably, the intermediate characteristic peak of Ti_2Ag_2 becomes distinctly observable only from an electrode potential of approximately −1.1 V, while the characteristic peaks of $Ti_{12}Ag_{4.5}$ are already evident at −0.5 V. This observation indicates that $Ti_{12}Ag_{4.5}$ demonstrates a higher reaction activity and stronger catalytic proficiency for the eCO$_2$RR, aligning with experimental findings.

Density Functional Theory (DFT) calculations were conducted to elucidate the reactivity of two specifically designed clusters, $Ti_{12}Ag_{4.5}$ and Ti_2Ag_2. These models were optimized to mirror their actual crystal structures, simplified by replacing the *tert*-butyl groups on the TC4A with H for faster computational convergence. The results of these optimizations are depicted in the Gibbs free energy diagrams for both the eCO$_2$RR and the HER, as presented in Fig. 7A. DFT calculations specifically focused on the energetics of each step, revealing that the formation of the *COOH intermediate is the rate-determining step in the CO$_2$RR process. A critical finding from our study is the calculated Gibbs free energy for the formation of *COOH on the Ag3 site in $Ti_{12}Ag_{4.5}$, which was notably low at 0.55 eV. This value contrasts with the corresponding energy of 0.88 eV for the same process within Ti_2Ag_2. This substantial difference highlights that the exposed Ag sites on $Ti_{12}Ag_{4.5}$ are much more energetically favorable for catalyzing the conversion of CO$_2$ to CO compared to those on bimetallic Ti_2Ag_2 (Fig. 7B). Additionally, the Gibbs free energies for hydrogen adsorption (*H) were calculated, showing high values of 2.46 eV for both clusters, indicating that neither Ti_2Ag_2 nor $Ti_{12}Ag_{4.5}$ is favorable for the formation of H$_2$. This finding is important as it underscores the higher selectivity of both clusters for the CO$_2$RR-to-CO pathway compared to the HER.

By comparing the Gibbs free energy diagrams of the eCO$_2$RR and HER, the exceptional catalytic efficiency of $Ti_{12}Ag_{4.5}$ is clearly linked to its unique Ag coordination. This coordination is supported by a titanium–oxo core, with Ag sites evenly distributed across the cluster surface. Specifically, the Ag active sites in $Ti_{12}Ag_{4.5}$ exhibit a d-band center (ε_d) that is closer to the Fermi level at −3.04 eV. As a comparison, the bimetallic cluster Ti_2Ag_2 exhibits a lower ε_d value of −3.47 eV, likely attributed to the absence of the unique support effects found in $Ti_{12}Ag_{4.5}$. Furthermore, the projected density of states (PDOS) for $Ti_{12}Ag_{4.5}$ shows higher and narrower peaks at energies near the Fermi level, suggesting a higher and more localized density of electronic states (Fig. S53†). This enhanced electronic configuration facilitates stronger interactions with adsorbate *COOH molecules, improving the activation and subsequent transformation of CO$_2$. These electronic characteristics are critical for reactions requiring complex electron interactions, thus positioning $Ti_{12}Ag_{4.5}$ as a more effective catalyst for CO$_2$ reduction.

Conclusions

In summary, this study has designed and synthesized a new type of crystalline oxide cluster-stabilized single-atom material that can more precisely emulate the structural and reactive characteristics of oxide-supported single-atom catalysts at the molecular level. We have discovered a solvent-mediated assembly process that transforms the calixarene-stabilized titanium oxide cluster, $Ti_{12}L_6$, into the oxide-supported cluster, $Ti_{12}Ag_{4.5}$. This transformed cluster prominently features six accessible single Ag^{1+} sites on its surface. The distinctive structure of $Ti_{12}Ag_{4.5}$ has demonstrated superior catalytic performance in the eCO$_2$RR, outperforming the traditional bimetallic cluster Ti_2Ag_2 in terms of reactivity and CO selectivity. *In situ* ATR-SEIRAS and DFT calculations were employed to investigate the catalytic mechanism, complemented by a structural comparison between $Ti_{12}Ag_{4.5}$ and Ti_2Ag_2 to clarify the factors underlying their different performances. These insights emphasize the importance of controlling the distribution of active metal sites on the surface of the cluster. This study promotes the intentional design of interactions between active surface sites and their cluster support, potentially establishing a new paradigm in single-atom catalyst design by significantly enhancing catalytic activities.

Data availability

The data that support the findings of this study are available in the main text and the ESI.†

Author contributions

C. L. supervised the project and conceived the idea. R. X. M., L. C. Z and L. K. W carried out synthesis, characterization and catalytic experiments of clusters. Q. T. and L. P. L performed the calculations for this article. Y.-L. S. was responsible for the
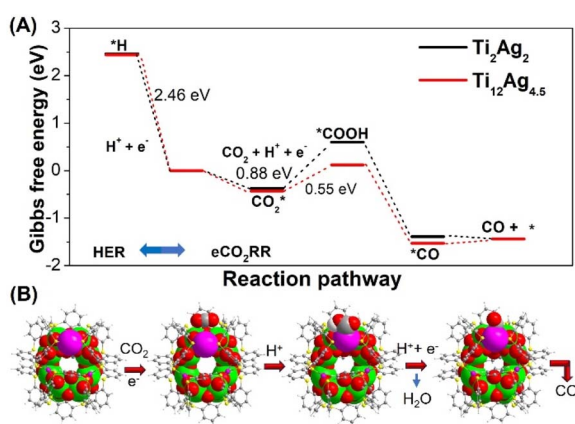

Fig. 7 (A) Free energy diagrams for the eCO$_2$RR and HER on $Ti_{12}Ag_{4.5}$ and Ti_2Ag_2; (B) schematic diagram of the eCO$_2$RR process on $Ti_{12}Ag_{4.5}$.

single crystal testing. C. L. wrote the manuscript. All authors discussed the experimental results.

Conflicts of interest

There are no conflicts of interest to declare.

Acknowledgements

Notes and references

1 L. Liu and A. Corma, *Chem. Rev.*, 2018, **118**, 4981–5079.
2 Y. Guo, S. Mei, K. Yuan, D. J. Wang, H. C. Liu, C. H. Yan and Y. W. Zhang, *ACS Catal.*, 2018, **8**, 6203–6215.
3 M. Murdoch, G. I. N. Waterhouse, M. A. Nadeem, J. B. Metson, M. A. Keane, R. F. Howe, J. Llorca and H. Idriss, *Nat. Chem.*, 2011, **3**, 489–492.
4 A. vonWeber and S. L. Anderson, *Acc. Chem. Res.*, 2016, **49**, 2632–2639.
5 B. Qiao, A. Wang, X. Yang, L. F. Allard, Z. Jiang, Y. Cui, J. Liu, J. Li and T. Zhang, *Nat. Chem.*, 2011, **3**, 634–641.
6 S. Yang, J. Kim, Y. J. Tak, A. Soon and H. Lee, *Angew. Chem., Int. Ed.*, 2016, **55**, 2058–2062.
7 J. Zhang, X. Wu, W. C. Cheong, W. Chen, R. Lin, J. Li, L. Zheng, W. Yan, L. Gu, C. Chen, Q. Peng, D. Wang and Y. D. Li, *Nat. Commun.*, 2018, **9**, 1002.
8 C. M. Zhao, X. Y. Dai, T. Yao, W. X. Chen, X. Q. Wang, J. Wang, J. Yang, S. Q. Wei, Y. Wu and Y. D. Li, *J. Am. Chem. Soc.*, 2017, **139**, 8078–8081.
9 J. D. Yi, X. P Gao, H. Zhou, W. Chen and Y. Wu, *Angew. Chem., Int. Ed.*, 2022, e202212329.
10 R. Lang, X. Du, Y. Huang, X. Jiang, Q. Zhang, Y. Guo, K. Liu, B. Qiao, A. Wang and T. Zhang, *Chem. Rev.*, 2020, **120**, 11986–12043.
11 X. F. Yang, A. Wang, B. Qiao, J. Li, J. Liu and T. Zhang, *Acc. Chem. Res.*, 2013, **46**, 1740–1748.
12 Z. Huang, X. Gu, Q. Cao, P. Hu, J. Hao, J. Li and X. Tang, *Angew. Chem., Int. Ed.*, 2012, **51**, 4198–4203.
13 C. T. Campbell, *Acc. Chem. Res.*, 2013, **46**, 1712–1719.
14 R. Jin, C. Zeng, M. Zhou and Y. Chen, *Chem. Rev.*, 2016, **116**, 10346–10413.
15 P. Liu, Y. Zhao, R. Qin, L. Gu, P. Zhang, G. Fu and N. Zheng, *Sci. Bull.*, 2018, **63**, 675–682.
16 W. H. Fang, L. Zhang and J. Zhang, *Chem. Soc. Rev.*, 2018, **47**, 404–421.
17 P. Coppens, Y. Chen and E. Trzop, *Chem. Rev.*, 2014, **114**, 9645–9661.
18 L. Rozes and C. Sanchez, *Chem. Soc. Rev.*, 2011, **40**, 1006–1030.
19 Y. Lv, J. Cheng, A. Steiner, L. Gan and D. S. Wright, *Angew. Chem., Int. Ed.*, 2014, **53**, 1934–1938.
20 C. Zhao, Y. Z. Han, S. Dai, X. Chen, J. Yan, W. Zhang, H. Su, S. Lin, Z. Tang, B. K. Teo and N. Zheng, *Angew. Chem., Int. Ed.*, 2017, **56**, 16252–16256.
21 G. Zhang, C. Liu, D. L. Long, L. Cronin, C. H. Tung and Y. Wang, *J. Am. Chem. Soc.*, 2016, **138**, 11097–11100.
22 W. H. Fang, L. Zhang and J. Zhang, *J. Am. Chem. Soc.*, 2016, **138**, 7480–7483.
23 M. Y. Gao, F. Wang, Z. G. Gu, D. X. Zhang, L. Zhang and J. Zhang, *J. Am. Chem. Soc.*, 2016, **138**, 2556–2559.
24 J. L. Hou, N. H. Huang, D. Acharya, Y. X. Liu, J. Y. Zhu, J. X. Teng, Z. Wang, K. Q. Qu, X. X. Zhang and D. Sun, *Chem. Sci.*, 2024, **15**, 2655–2664.
25 M. Zhang, M. Lu, M.-Y. Yang, J.-P. Liao, Y.-F. Liu, H.-J. Yan, J.-N. Chang, T.-Y. Yu, S.-L. Li and L. Y. Qian, *eScience*, 2023, **3**, 100116.
26 Y. J. Liu, P. Shao, M. Y. Gao, W. H. Fan and J. Zhang, *Inorg. Chem.*, 2020, **59**, 11442–11448.
27 X. Fan, F. Yuan, D. Li, S. Chen, Z. Cheng, Z. Zhang, S. Xiang, S. Q. Zang, J. Zhang and L. Zhang, *Angew. Chem., Int. Ed.*, 2021, **60**, 12949–12954.
28 M. Y. Gao, K. Wang, Y. Y. Sun, D. J. Li, B. Q. Song, Y. H. Andaloussi, M. J. Zaworotko, J. Zhang and L. Zhang, *J. Am. Chem. Soc.*, 2020, **142**, 12784–12790.
29 N. Li, J.-M. Lin, R.-H. Li, J.-W. Shi, L.-Z. Dong, J. Liu, J. He and Y. Q. Lan, *J. Am. Chem. Soc.*, 2023, **145**, 16098–16108.
30 E. M Han, R. X Meng, Y. Q Tian, J. Yan, K. Y Liu and C. Liu, *Chem. Commun.*, 2023, **59**, 11097–11100.
31 S. Chen, Z. N. Chen, W. H. Fang, W. Zhuang, L. Zhang and J. Zhang, *Angew. Chem., Int. Ed.*, 2019, **58**, 10932–10935.
32 D. T. Geng, X. Han, Y. F. Bi, Y. C. Qin, Q. Li, L. L. Huang, K. Zhou, L. J. Song and Z. P. Zheng, *Chem. Sci.*, 2018, **9**, 8535–8541.
33 S. T. Wang, X. H. Gao, X. X. Hang, X. F. Zhu, H. T. Han, W. P. Liao and W. Chen, *J. Am. Chem. Soc.*, 2016, **138**, 16236–16239.
34 Y. Q. Tian, W. L. Mu, L. L. Wu, X. Y. Yi, J. Yan and C. Liu, *Chem. Sci.*, 2023, **14**, 10212–10218.
35 Z. Wang, L. Li, L. Feng, Z. Y. Gao, C. H. Tung, L. S. Zheng and D. Sun, *Angew. Chem., Int. Ed.*, 2022, **61**, e202200823.
36 Z. Wang, H. F. Su, Y. W. Gong, Q. P. Qu, Y. F. Bi, C. H. Tung, D. Sun and L. S. Zheng, *Nat. Commun.*, 2020, **11**, 308.
37 Z. Wang, F. Alkan, C. M. Aikens, M. Kurmoo, Z. Y. Zhang, K. P. Song, C. H. Tung and D. Sun, *Angew. Chem., Int. Ed.*, 2022, **61**, e202206742.
38 Z. J. Guan, F. Hu, S. F. Yuan, Z. A. Nan, Y. M. Lin and Q. M. Wang, *Chem. Sci.*, 2019, **10**, 3360–3365.
39 X.-M. Luo, S. Huang, P. Luo, K. Ma, Z.-Y. Wang, X.-Y. Dong and S.-Q. Zang, *Chem. Sci.*, 2022, **13**, 11110–11118.
40 L. J. Li, Y. T. Luo, Y. Q. Tian, P. Wang, X. Y. Yi, J. Yan, Y. Pei and C. Liu, *Inorg. Chem.*, 2023, **62**, 14377–14384.
41 Z. Liu, J. Chen, B. Li, D.-e. Jiang, L. Wang, Q. Yao and J. Xie, *J. Am. Chem. Soc.*, 2024, **146**(17), 11773–11781.
42 S. L. Zhuang, D. Chen, L. W. Liao, Y. Zhao, N. Xia, W. Zhang, C. Wang, J. Yang and Z. Wu, *Angew. Chem., Int. Ed.*, 2020, **59**, 3073–3077.

43 J. Y. Xu, L. Xiong, X. Cai, S. S. Tang, A. C. Tang, X. Liu, Y. Pei and Y. Zhu, *Chem. Sci.*, 2022, **13**, 2778–2782.

44 X. Liu, E. D. Wang, M. Zhou, Y. Wan, Y. K. Zhang, H. Q. Liu, Y. Zhao, J. Li, Y. Gao and Y. Zhu, *Angew. Chem., Int. Ed.*, 2022, **61**, e202207685.

45 S. Li, A. V. Nagarajan, D. R. Alfonso, M. K. Sun, D. R. Kauffman, G. Mpourmpakis and R. Jin, *Angew. Chem., Int. Ed.*, 2021, **60**, 6351–6356.

46 S. Zhao, N. Austin, M. Li, Y. Song, S. D. House, S. Bernhard, J. C. Yang, G. Mpourmpakis and R. Jin, *ACS Catal.*, 2018, **8**, 4996–5001.

47 L. Tang, Y. Luo, X. Ma, B. Wang, M. Ding, R. Wang, P. Wang, Y. Pei and S. Wang, *Angew. Chem., Int. Ed.*, 2023, e202300553.

48 L. J. Li, W. L. Mu, Y. Q. Tian, W. D. Yu, L. Y. Li, J. Yan and C. Liu, *Chem. Sci.*, 2024, **15**, 7643–7650.

49 G. C. Deng, H. Yun, M. S. Bootharaju, F. Sun, K. Lee, X. L. Liu, S. Yoo, Q. Tang, Y. J. Hwang and T. Hyeon, *J. Am. Chem. Soc.*, 2023, **145**(50), 27407–27414.

50 L. B. Qin, F. Sun, X. S. Ma, G. Y. Ma, Y. Tang, L. Wang, Q. Tang, R. Jin, Z. Tang and Z. H. Tang, *Angew. Chem., Int. Ed.*, 2021, **60**, 26136–26141.

51 X. S. Ma, F. Sun, L. B. Qin, Y. G. Liu, X. W. Kang, L. K. Wang, D. E. Jiang, Q. Tang and Z. H. Tang, *Chem. Sci.*, 2022, **13**, 10149–10158.

52 S. Yoo, S. Yoo, G. C. Deng, F. Sun, K. Lee, H. Jang, C. W. Lee, X. L. Liu, J. Jang, Q. Tang, Y. J. Hwang, T. Hyeon and M. S. Bootharaju, *Adv. Mater.*, 2024, **36**, 2313032.

53 X. L. Liu, T. Ki, G. C. Deng, S. Yoo, K. Lee, B.-H. Lee, T. Hyeon and M. S. Bootharaju, *Nanoscale*, 2024, **16**, 12329–12344.

54 G. Deng, J. Kim, M. S. Bootharaju, F. Sun, K. Lee, Q. Tang, Y. J. Hwang and T. Hyeon, *J. Am. Chem. Soc.*, 2023, **145**, 3401–3407.

55 J. Wang, F. Xu, Z. Y. Wang, S. Q. Zang and T. C. W. Mak, *Angew. Chem., Int. Ed.*, 2022, **61**, e202207492.

56 L. J. Liu, Z. Y. Wang, Z. Y. Wang, R. Wang, S. Q. Zang and T. C. Mak, *Angew. Chem., Int. Ed.*, 2022, **61**, e202205626.

57 Y. F. Lu, L. Z. Dong, J. Liu, R. X. Yang, J. J. Liu, Y. Zhang, L. Zhang, Y. R. Wang, S. L. Li and Y. Q. Lan, *Angew. Chem., Int. Ed.*, 2021, **60**, 26210–26217.

58 D. Wang, J. J. Mao, C. C. Zhang, J. W. Zhang, J. S. Li, Y. Zhang and Y. F. Zhu, *eScience*, 2023, **3**, 100119.

59 X. Wang, M. H. Yu and X. L. Feng, *eScience*, 2023, **3**, 100141.